• Article •

Single-shot real-time imaging of ultrafast light springs

Chengzhi Jin[1†], Dalong Qi[1†], Yunhua Yao[1], Fengyan Cao[1], Li Deng[2], Shixiang Xu[3],
Zhenrong Sun[1], and Shian Zhang[1,4,5*]

[1]*State Key Laboratory of Precision Spectroscopy, School of Physics and Electronic Science, East China Normal University, Shanghai 200241, China;*
[2]*School of Physics and Electronic Science, East China Normal University, Shanghai 200241, China;*
[3]*Shenzhen Key Laboratory of Micro-Nano Photonic Information Technology, College of Physics and Optoelectronics Engineering,
Shenzhen University, Shenzhen 518060, China;*
[4]*Collaborative Innovation Center of Extreme Optics, Shanxi University, Taiyuan 030006, China;*
[5]*Collaborative Innovation Center of Light Manipulations and Applications, Shandong Normal University, Jinan 250358, China*

Light springs (LSs) have played essential roles in particle rotation and manipulation, optical super-resolution imaging, and optical information coding. In related research areas, it is important to accurately measure spatiotemporal information on LSs to understand and analyze their applications. However, there is no experimental method that can accurately detect the drastic spatial evolution of ultrafast LSs to date. Therefore, in this study, we propose a compressed ultrafast photography (CUP) technique to observe LSs in spatial and temporal dimensions with a snapshot. Using our home-built CUP system, we successfully capture spatiotemporal information on picosecond LSs with two and four petals, involving spatial structure and rotation velocity; furthermore, the experimental measurements are in good agreement with theoretical simulations. This study provides a novel visualization method for specifically measuring the spatial structure and temporal evolution of LSs, thus establishing a new idea for accurately characterizing spatiotemporal information on complex ultrafast laser fields.

spatio-temporal light springs, compressed ultrafast photography, computational imaging, single shot

PACS number(s):   42.25.Bs, 42.30.Va, 42.30.Wb, 95.75.Mn

1   Introduction

Light springs (LSs), as a type of novel-shaped ultrafast laser beam carrying orbital angular momentum (OAM), have a helical structure in both phase and intensity profile [1-3]. Because of unique properties, LSs have attracted attention in particle rotation and manipulation [4-6], optical super-

resolution imaging [7], and optical information coding [8,9]. Among these pioneering studies, Paterson et al. [4] used a rotating glass plate to generate LSs with a 5-Hz rotational frequency and successfully applied it to the rotational manipulation of microscopic particles, which provided a method for precisely manipulating biological molecules such as orienting DNA strands. By controlling the intensity distribution and azimuth angle of LSs, Yang et al. [8] added a degree of freedom in optical information coding that could

---

*Corresponding author (email: sazhang@phy.ecnu.edu.cn)
† These authors contributed equally to this work

significantly increase the information transmission capacity, which provided a promising technique for solving problems of insufficient communication capacity. Recently, Krüger et al. [7] applied LSs to tomographic stimulated emission depletion microscopy; compared with traditional gaussian-type structured light, the rotationally symmetric structured light can considerably reduce the luminescence threshold intensity and photobleaching of biological samples. These applications of LSs have increased demands on precision control and measurement. Usually, LSs can be obtained by superimposing Laguerre-Gaussian (LG) beams where the azimuthal mode indexes correlate with their frequencies. Multiple approaches have been proposed to generate LSs, primarily via a modulation strategy using spatial light modulator [10], acousto-optic modulator [11], axially symmetric polarization elements [12], or Michelson interferometer (MI) [13]. Among these approaches, the MI-based strategy is easy to adjust the topological charges (TCs) of LG beams as well as the rotation velocity of the wavefront; therefore, it is convenient and flexible to generate LSs with multiple azimuthal intensity helixes and rotation velocities. Certain experimental methods have attempted to quantitatively characterize the spatiotemporal information on LSs; however, all these methods show distinct deficiencies. For example, a pump-probe scheme-based time-resolved sum-frequency generation (SFG) imaging method [2] cannot detect single pulses; therefore, it is invalid to sense variations in different pulses. Ultrafast framing cameras [14] cannot obtain complete spatiotemporal information on LSs because of the small sequence depth (i.e., the number of frames per exposure). To our knowledge, an experimental method that can completely detect the drastic spatial evolution behavior of ultrafast LSs does not exist. To address the abovementioned issues, we proposed a compressed ultrafast photography (CUP) [15, 16] technique to realize the single-shot real-time spatiotemporal detection of ultrafast LSs.

To date, multiple technical approaches have been developed for ultrafast snapshot temporal imaging such as sequentially timed all-optical mapping photography (STAMP) [17], frequency-domain tomography (FDT) [18], frequency recognition algorithm for multiple exposures (FRAME) [19], ultrafast all-optical solid-state framing camera (UASFC) [20], single-shot imaging technique based on spatial/temporal division and routing (STDR) [21], time and spatial-frequency multiplexing (TSFM) [22], and CUP. All these imaging schemes have their advantages and disadvantages; both STEAM and FRAME are active imaging technologies, preventing them from measuring the self-emission ultrafast processes, whereas FDT, UASFC, STDR, and TSFM depend on the number of beam splitters, thereby requiring high luminous flux, and the total number of frames is usually no larger

than 10. CUP combines streak imaging [23] and compressed sensing [24], which is a receive-only snapshot imaging technology; therefore, it is suitable for recording nonrepeatable or irreversible transient events [25-27]. In CUP, the dynamic scene is encoded in space and sheared in time. Subsequently, the modulated dynamic scene is integrally recorded by a 2D array device. Finally, the original dynamic scene can be recovered from the 2D image via image reconstruction. Owing to the excellent performance of CUP in both imaging speed and sequence depth, it has been successfully employed to observe multiple transient optical scenes such as capturing flying photons [28], recording moving volumetric objects [29], imaging the spatiotemporal dynamics of plasma [25], observing optical chaos [27], and dissipative soliton dynamics [30].

In this study, two vortex retarders with different TCs and an asymmetric MI are designed to generate picosecond LSs with two or four petals; then, CUP is employed to capture ultrafast LSs with snapshot; finally, a fast and flexible denoising convolutional neural network (FFDNet)-based plug-and-play (PnP) alternating direction method of multiplier (ADMM) framework algorithm (ADMM-FFDNet) is employed to reconstruct the original ultrafast LSs [31-34]. The results agree with the theoretical calculations in both the spatial structure and rotation velocity of LSs, which confirm that CUP can realize the single-shot real-time imaging of ultrafast LSs. The precise measurement of spatiotemporal information on LSs is important for advancing their applications in the abovementioned areas, as well as generating isolated strong half-cycle pulses in the field of attosecond science [35], and verifying the exchange of OAM between laser light and matter at relativistic intensity areas [36], and so on.

2 Principles of LSs and CUP

2.1 Principle of LSs

For the MI-based method, LSs are obtained by overlapping two temporally chirped vortex pulses with different instantaneous frequencies and TCs in space and time [2, 13]. The vortex optical field is generated using a vortex retarder sandwiched by two quarter-waveplates; it can be expressed as follows [37, 38]:

$$E_l(r, \theta, \omega, t) = E(r, \theta)E(t)\exp(il\theta)\exp(i\omega t), \qquad (1)$$

where l is the TC, ω is the instantaneous frequency of the optical field, $E(t)$ is the Fourier transform of $E(\omega)$, and $E(r, \theta)$ is the space-dependent complex amplitudes. $E(r, \theta)$ is deter-

mined as follows:

$$E(r, \theta) = E_{z=0}^l(r, \theta) = \left(\frac{2}{\pi |l|!}\right)^{\frac{1}{2}} \frac{1}{w} \left(\frac{r\sqrt{2}}{w}\right)^{|l|} \exp\left(\frac{-r^2}{w^2}\right), \qquad (2)$$

where w denotes the beam radius. Considering two vortex beams $E_{l_1}(r, \theta, \omega_1, t)$ and $E_{l_1}(r, \theta, \omega_2, t)$ with different TCs, the beat frequency $\delta\omega$ is $\delta\omega = \omega_1 - \omega_2$ when $\omega_0 = (\omega_1 + \omega_2)/2$. Thus, the LSs can be written as follows:

$$\begin{aligned}
E(r, \theta, t) &= E_{l_1}(r, \theta, \omega_1, t) + E_{l_2}(r, \theta, \omega_2, t) \\
&= \left[E_1(r, \theta)E_1(t) \exp\left(il_1\theta - i\frac{\delta\omega}{2}t\right)\right. \\
&\quad \left. + E_2(r, \theta)E_2(t) \exp\left(il_2\theta + i\frac{\delta\omega}{2}t\right)\right] \exp(i\omega_0 t).
\end{aligned} \quad (3)$$

From eq. (3), the finally formed optical field has a symmetrical structure, which is jointly determined by l_1 and l_2 and its symmetry axis periodically changes. Once $E(r, \theta, t)$ is set to 0, the angular velocity Ω is formulated by considering the derivative of t with respect to θ as follows:

$$\Omega = \frac{\mathrm{d}\theta}{\mathrm{d}t} = \frac{\delta\omega}{|l_1 - l_2|}. \qquad (4)$$

For ultrafast chirped pulse generated by dispersive elements, the relationship between ω and t can be expressed as $\omega(t) = Ct + \omega_0$, where C is the chirp coefficient [39, 40], which is an inherent property of the chirped pulse; it can be determined by the transform-limited pulse width τ_0 and chirp pulse width τ as follows:

$$C \approx \frac{4\ln(2)}{\tau^2} \sqrt{\frac{\tau^2}{\tau_0^2} - 1}. \qquad (5)$$

Thus, the beat frequency $\delta\omega$ can be written as $\delta\omega = \omega(t) - \omega(t - \delta t) = C\delta t$, where δt is the time delay between the two chirped vortex pulses in the MI system. Finally, Ω can be simplified as follows:

$$\Omega = \frac{C\delta t}{|l_1 - l_2|}. \qquad (6)$$

Furthermore, the rotation period T can be written as follows:

$$T = \frac{2\pi |l_1 - l_2|}{\delta\omega} = \frac{2\pi |l_1 - l_2|}{C\delta t}. \qquad (7)$$

Based on eq. (7), the following can be concluded: (1) the smaller $|l_1 - l_2|$, the smaller T; (2) the smaller δt, the larger T. When δt is 0, the symmetrical structure of LSs will be fixed, which can be used to determine time zero of two chirped vortex pulses.

2.2 Principle of CUP

In CUP, the entire operation process can be divided into two parts: data acquisition and image reconstruction. In the data acquisition, a dynamic scene is spatially encoded by a digital micromirror device (DMD), temporally sheared by a streak camera, and integrally measured by a complementary metaloxide-semiconductor (CMOS). The obtained 2D image can be mathematically formulated as follows [15]:

$$E(m, n) = TSCI(x, y, t), \qquad (8)$$

where $I(x, y, t)$ represents the intensity distribution of the vortex laser field, i.e., the picosecond LSs in this study; C, S, and T are spatial encoding, temporal shearing, and spatiotemporal integration operators, respectively; $E(m, n)$ is the intensity distribution detected by CMOS. For simplicity, set $A = TSC$; thus, eq. (8) can be rewritten as follows:

$$y = Ax + n, \qquad (9)$$

where $A \in \mathbb{R}^{WH \times WHB}$ is the measurement matrix, $y \in \mathbb{R}^{W \times H}$ is the measurement value obtained by sampling, $x \in \mathbb{R}^{W \times H \times B}$ is the datacube of dynamic scene, and n denotes the measurement and sensor noise in the image acquisition process; W and H are the width and height of image sensor, respectively.

For image reconstruction, the original dynamic scene needs to be recovered as faithfully as possible from the acquired 2D image, which is an under-determined optimization problem. One technique to solve the optimization problem is by introducing prior information or assumptions. In this study, an ADMM-FFDNet algorithm is employed to obtain the approximate result by solving the following problems [32]:

$$(\hat{x}, \hat{v}) = \mathrm{argmin}_{x,v} f(x) + \lambda g(v), \text{ subject to } x = v, \qquad (10)$$

where $f(x)$ is the objective function, λ is the regularization parameter, $g(v)$ is the regularization function, and v is an auxiliary variable. The regularization parameter λ can be adjusted to guide the reconstruction results with almost identical physical reality. This problem can be solved by figuring out the following series of subproblems:

$$x^{(k+1)} = \mathrm{argmin}_x f(x) + \frac{\rho}{2} \left\| x - \left(v^{(k)} - \frac{1}{\rho}u^{(k)}\right) \right\|_2^2, \qquad (11)$$

$$v^{(k+1)} = \mathrm{argmin}_v \lambda g(v) + \frac{\rho}{2} \left\| v - \left(x^{(k)} + \frac{1}{\rho}u^{(k)}\right) \right\|_2^2, \qquad (12)$$

$$u^{(k+1)} = u^{(k)} + \rho\left(x^{(k+1)} - v^{(k+1)}\right), \qquad (13)$$

where the superscript k represents the number of iterations, which should be less than the total number of iterations N, and ρ is a penalty parameter introduced by ADMM [41]. The

FFDNet is used as the image denoiser; thus, the solution of eq. (12) can be written as follows:

$$\boldsymbol{v}^{(k+1)} = \mathcal{D}_{\text{FFDNet}}\left(\boldsymbol{x}^{(k+1)} + \frac{1}{\rho}\boldsymbol{u}^{(k)}\right), \tag{14}$$

where $\mathcal{D}_{\text{FFDNet}}$ indicates the FFDNet denoiser. In the PnP framework [42], an inverse problem is regularized using a deep learning denoiser within the ADMM iterative algorithm. The entire flowchart of image reconstruction is shown in Figure 1.

3   Experimental design

An experimental arrangement for imaging LSs via CUP is shown in Figure 2. In an LS component, a mode-locked Ti:Sapphire laser amplifier is employed to generate a temporally chirped pulse with about 40-ps pulse width and an 800-nm central wavelength. The output chirped pulse is converted into the vortex pulse by passing through two quarter-waveplates (Q1 and Q2) and a vortex retarder (V), where the vortex retarder is placed between the two quarter-waveplates; then, a Glan prism (P) is used to ensure that the vortex pulse is linearly polarized. To generate a pair of vortex subpulses with conjugated TCs, the vortex pulse is divided into two subpulses by a beam splitter (BS1) and then passed through an asymmetric MI with three mirrors (M1-3) in one arm and a retro-reflecting prism (RP) in the other arm, where the time delay between the two subpulses can be precisely controlled

Figure 1   (Color online) Flowchart of image reconstruction based on ADMM-FFDNet algorithm.

by a linear-piezo-motor driven delay stage. When the pair of vortex subpulses are combined by the second beam splitter (BS2), LSs are successfully generated. Furthermore, the petals of LSs can be conveniently manipulated by designing the TCs of two vortex retarders.

In the CUP component, the generated LSs, as the dynamic scene, are imaged on a DMD via two 4f imaging systems where each imaging system comprises a couple of lenses (L1-2 or L3-4). The dynamic scene is spatially encoded by the DMD, which consists of millions of micromirrors, and each micromirror can be individually tilted into 12 as "on" or "off" states. A pseudorandomly distributed binary pattern is loaded on the DMD as the mask. The encoded dynamic scene reflected from "on" micromirrors is collected by the second 4f imaging system (L3-4), then reflected by another beam splitter (BS3), and finally integrally measured by a streak camera (Hamamatsu, C7700) with the slit being fully opened.

4   Results and discussion

From eqs. (6) and (7), the rotation period T or the angular velocity Ω was determined by δt and $|l_1 - l_2|$. In our experiment, the TCs of the vortex retarders were 1 and 2, respectively. Limited by the imaging speed of 500 billion frames per second (fps) in our CUP system [43], which could not observe the ultrafast dynamic scene within 2 ps. Therefore, to ensure that the rotation velocity in the pulse width $\tau = 40$ ps could be clearly observed, $\delta t < 145$ fs for $l_1 = -l_2 = 1$ and $\delta t < 290$ fs should be satisfied for $l_1 = -l_2 = 2$, respectively. Moreover, the rotation direction could be switched by controlling the time order of two vortex subpulses. In this study, we used the two vortex retarders with the TCs of 1 and 2 to generate two- and four-petal LSs and then measured the rotation velocities and directions of two LSs by controlling the time interval and order of two vortex subpulses.

4.1   Imaging two-petal LSs

First, the two-petal LSs were generated by employing the two vortex subpulses with conjugated TCs of 1 and −1 at the time delays of 30 and 100 fs, respectively. After data acquisition and image reconstruction, the representative reconstructed results are shown in Figure 3(a) and (c). A total of 16 frames are given, and the temporal interval between two adjacent frames is 4 ps. The two-petal structure in each frame can be observed. Moreover, the two-petal LSs show the counterclockwise rotation. For comparison, the spatiotemporal evolutions of LSs were also theoretically simulated using eq. (3) based on the experimental parameters, where $E_1(r, \theta)E_1(t)$
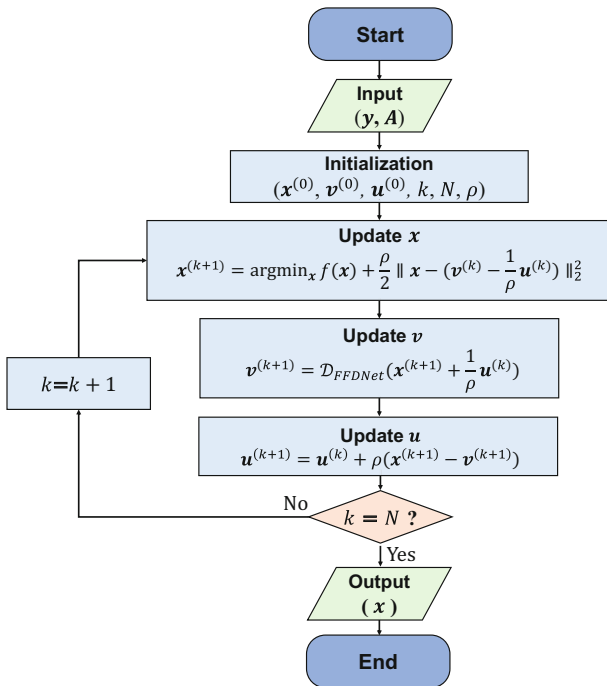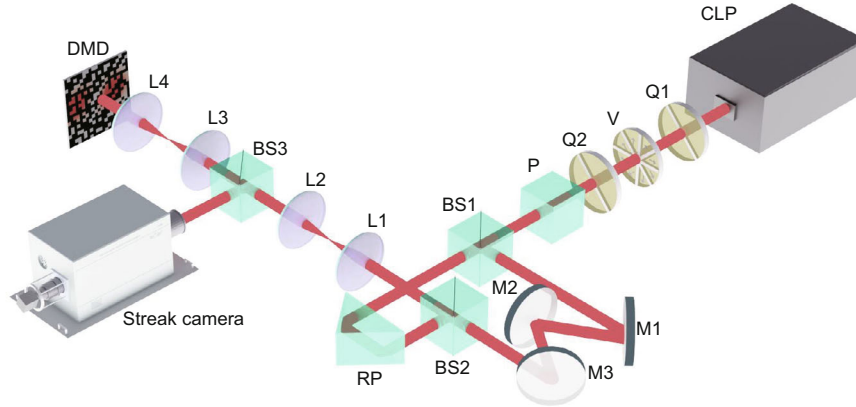
Figure 2   (Color online) Experimental design for imaging LSs via CUP, where CLP: chirped laser pulses; Q1-Q2: quarter-waveplates; V: vortex retarder; P: Glan prism; RP: retro-reflecting prism; M1-M3: mirrors; BS1-BS3: beam splitters; L1-L4: lenses; DMD: digital micromirror device.
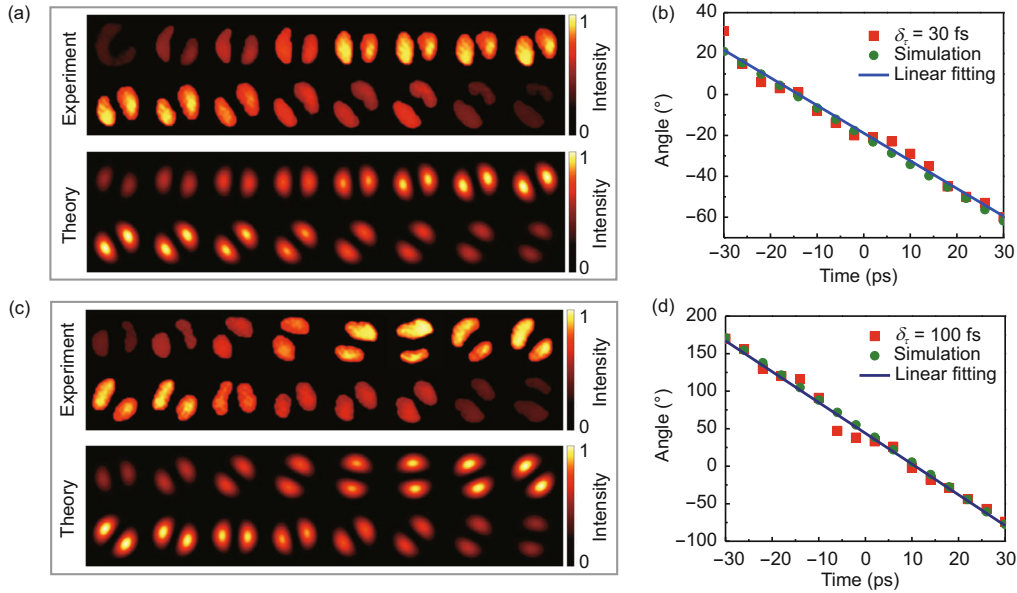

Figure 3   (Color online) Imaging two-petal LSs. (a), (c) Experimental and theoretical results with the time delays of 30 and 100 fs, respectively; (b), (d) extracted time-dependent rotation angles from (a) and (c), respectively, together with linear fitting. Two spatiotemporal evolution movies of two-petal LSs corresponding to the time delays are provided in visualizations 1 and 2 (see Supporting Information).

was set to be equal to $E_2(r, \theta)E_2(t)$. Similarly, a total of 16 frames with the temporal frame interval of 4 ps are also given in Figure 3(a) and (c). The experimental results agreed with the theoretical simulations, both in the structures and intensities in the spatiotemporal evolutions. In addition, the two petals showed good symmetry at the time delay of 30 fs, whereas the symmetry worsened at the time delay of 100 fs due to the faster rotation speed.

To quantitatively achieve rotation-related velocity, a log-polar transform-based matching algorithm [44, 45] was employed to calculate the angle between the imaginary axial and vertical lines in each frame; both experimental and theoretical results are shown in Figure 3(b) and (d) for the time

delays of 30 and 100 fs, respectively, along with linear fitting. The experimental results agreed well with the theoretical simulations. Based on Figure 3(b) and (d), the rotation velocities were calculated using eq. (6); the calculation results are shown in Table 1. At the 30-fs time delay, the rotation velocities were 1.28 and 1.24°/ps for the experimental measurement and theoretical simulation, respectively, and their relative error was only 3.23%. When the time delay increased to 100 fs, the experimental and theoretical rotation velocities were, respectively, 4.10 and 4.14°/ps, and the relative error was 0.98%, which was insignificant. The rotation velocity at the time delay of 100 fs was about three times that at the time delay of 30 fs, which completely agreed with the

theoretical model prediction.

4.2   Imaging four-petal LSs

The four-petal LSs were generated via the same strategy using the two vortex subpulses with conjugated TCs of 2 and −2 at the time delays of −40 and −80 fs, respectively. The minus sign represents the opposite time order between the two vortex subpulses compared with that in Figure 3. Similarly, Figure 4(a) and (c) show a total of 16 frames with 4-ps temporal frame interval for reconstructed results and theoretical simulations, respectively. Similar to Figure 3, the evolution of the spatial structure for the four-petal LSs could be observed, which demonstrated the robust performance of CUP in measuring the vortex light field. Furthermore, by switching the time order of the two vortex subpulses, the four-petal LSs demonstrated a clockwise rotation, which was the opposite of the two-petal LSs in Figure 3. Note that the spatial symmetry of the four-petal structure was worse than that of the two-petal LSs, which should be attributed to the more rigorous requirements for generating the four-petal LSs in the spatial overlap of the two vortex subpulses. This deformation would be submerged in the rotation of LSs, which was difficult to recognize using conventional detectors. Moreover, any small vibration in the experiment would induce an obvious spatial distortion, which demonstrated the relevance of the spatiotemporal dynamic measurement of LSs with a snapshot.

Furthermore, similar algorithms were employed to calculate the rotation angles of Figure 4(a) and (c); the calculation results are given in Figure 4(b) and (d). Moreover, the experimental results and theoretical simulations agreed. The rotation velocities of four-petal LSs were calculated (Table 2). When the time delay was set to −40 fs, the experimental rotation velocity was −0.83°/ps, which was exactly the same as the theoretical value. When the time delay was adjusted to −80 fs, which was two times as much as −40 fs, the experimental rotation velocity increased to −1.62°/ps; furthermore, the relative error was only 1.85% compared with the theoretical value of −1.65°/ps.

As reported previously, both two- and four-petal LSs measured by CUP demonstrated high-quality consistency with theoretical simulations. Owing to the high data compression ratio of CUP, the reconstructed images had some degree of smoothness and distortion; however, compared with other detection methods such as time-resolved SFG imaging [2]

Table 1   The rotation velocities of two-petal LSs at different time delays

Time delay	Experiment (°/ps)	Theory (°/ps)	Relative error (%)
$\delta t = 30$ fs	1.28	1.24	3.23
$\delta t = 100$ fs	4.10	4.14	0.98

Table 2   The rotation velocities of four-petal LSs at different time delays

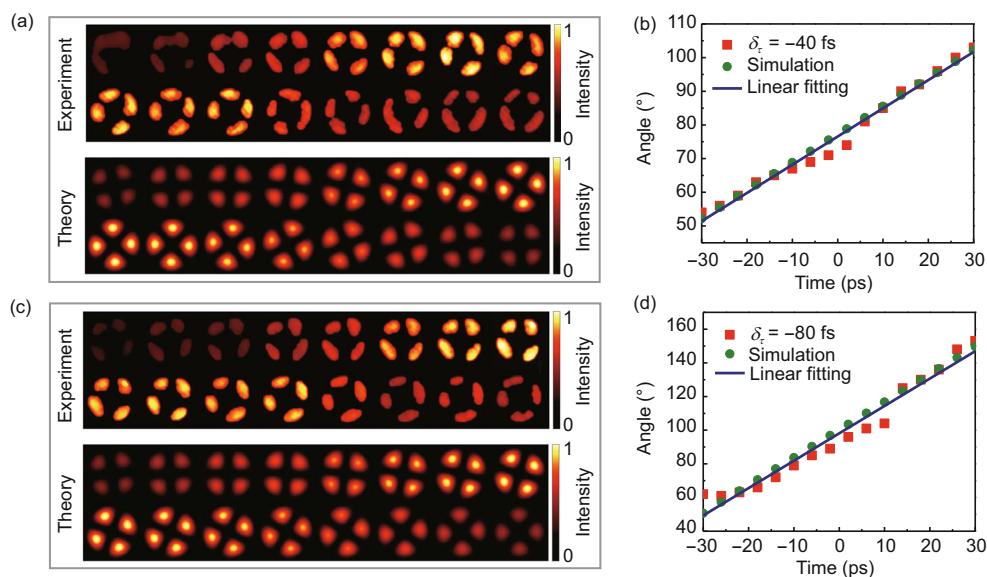| Time delay	Experiment (°/ps)	Theory (°/ps)	Relative error (%)
$\delta t = -40$ fs	−0.83	−0.83	0
$\delta t = -80$ fs	−1.62	−1.65	1.85

Figure 4   (Color online) Imaging of four-petal LSs. (a), (c) Experimental and theoretical results with time delays of −40 and −80 fs, respectively; (b), (d) extracted time-dependent rotation angles from (a) and (c), respectively, along with linear fitting. Two spatiotemporal evolution movies of four-petal LSs corresponding to time delays are provided in visualizations 3 and 4 (see Supporting Information).

or ultrafast framing imaging based on noncollinear optical parametric amplification [14], CUP could obtain the entire spatiotemporal details of LSs because of a large sequence depth; this demonstrated the unprecedented advantages in ultrafast laser field measurements. By optimizing the CUP system and image reconstruction algorithm further, the measurement accuracy of CUP could be improved, e.g., using an electro-optic deflector rather than a streak camera, image distortion induced by the Coulomb interaction of electrons could be eliminated [46]. In image reconstruction, the results considerably depended on the quality of the image measured on the detector. Furthermore, seeking additional optimized image reconstruction algorithms of CUP has always been the aim of researchers in this area.

5 Conclusions

In summary, we experimentally generated spatiotemporal LSs using two vortex pulses based on an asymmetric MI strategy and successfully measured the spatial structures and rotation velocities of two- and four-petal LSs by CUP. Our results agreed well with the theoretical simulations, which showed the excellent performance of CUP in measuring complex vortex laser fields. In CUP, the imaging speed was limited by the temporal resolution of a streak camera. In this experiment, the maximal rotation frequency of LSs was about 10 GHz. By employing the state-of-the-art streak camera (Hamamatsu, C6138), the imaging speed of CUP could reach 70 trillion fps [26]; thus, CUP could image the LSs rotating at the frequency of THz (i.e., THz LSs). The THz LSs have crucial roles in detecting the spatial structure or functional evolution of biomolecules [47-49]. In the future, CUP can provide a well-established tool to detect the interaction of THz LSs and biomolecules as well as explore its mechanism.

Supporting Information

The supporting information is available online at phys.scichina.com and link.springer.com. The supporting materials are published as submitted, without typesetting or editing. The responsibility for scientific accuracy and content remains entirely with the authors.

1 G. Pariente, and F. Quéré, Opt. Lett. **40**, 2037 (2015).
2 K. Yamane, M. Sakamoto, N. Murakami, R. Morita, and K. Oka, Opt. Lett. **41**, 4597 (2016).
3 Y. Shi, J. Vieira, R. M. G. M. Trines, R. Bingham, B. F. Shen, and R. J. Kingham, Phys. Rev. Lett. **121**, 145002 (2018), arXiv: 1802.08582.
4 L. Paterson, Science **292**, 912 (2001).
5 W. M. Lee, X. C. Yuan, and D. Y. Tang, Opt. Express **11**, 199 (2003).
6 Y. Cao, T. Zhu, H. Lv, and W. Ding, Opt. Express **24**, 3377 (2016).
7 J. R. Krüger, J. Keller-Findeisen, C. Geisler, and A. Egner, Biomed. Opt. Express **11**, 3139 (2020).
8 D. Yang, Y. Li, D. Deng, J. Ye, Y. Liu, and J. Lin, J. Phys. D-Appl. Phys. **52**, 495103 (2019).
9 J. Wang, Sci. China-Phys. Mech. Astron. **62**, 034201 (2019).
10 X. He, P. Xu, J. Wang, and M. Zhan, Opt. Express **17**, 21007 (2009).
11 S. Franke-Arnold, J. Leach, M. J. Padgett, V. E. Lembessis, D. Ellinas, A. J. Wright, J. M. Girkin, P. Öhberg, and A. S. Arnold, Opt. Express **15**, 8619 (2007), arXiv: physics/0611154.
12 M. Sakamoto, K. Oka, R. Morita, and N. Murakami, Opt. Lett. **38**, 3661 (2013).
13 X. Zeng, S. Zheng, Y. Cai, H. Wang, H. Lu, H. Wang, J. Li, W. Xie, and S. Xu, High Power Laser Sci. Eng. **8**, e3 (2020).
14 X. Zeng, S. Zheng, Y. Cai, Q. Lin, J. Liang, X. Lu, J. Li, W. Xie, and S. Xu, Adv. Photon. **2**, 56002 (2020).
15 L. Gao, J. Liang, C. Li, and L. V. Wang, Nature **516**, 74 (2014).
16 D. Qi, S. Zhang, C. Yang, Y. He, F. Cao, J. Yao, P. Ding, L. Gao, T. Jia, J. Liang, Z. Sun, and L. V. Wang, Adv. Photon. **2**, 14003 (2020).
17 K. Nakagawa, A. Iwasaki, Y. Oishi, R. Horisaki, A. Tsukamoto, A. Nakamura, K. Hirosawa, H. Liao, T. Ushida, K. Goda, F. Kannari, and I. Sakuma, Nat. Photon. **8**, 695 (2014).
18 Z. Li, R. Zgadzaj, X. Wang, Y. Y. Chang, and M. C. Downer, Nat. Commun. **5**, 3085 (2014).
19 A. Ehn, J. Bood, Z. Li, E. Berrocal, M. Aldén, and E. Kristensson, Light: Sci. Appl. **6**, 1 (2017).
20 G. Gao, K. He, J. Tian, C. Zhang, J. Zhang, T. Wang, S. Chen, H. Jia, F. Yuan, L. Liang, X. Yan, S. Li, C. Wang, and F. Yin, Opt. Express **25**, 8721 (2017).
21 S. Yeola, D. Kuk, and K. Y. Kim, J. Opt. Soc. Am. B **35**, 2822 (2018), arXiv: 1807.02111.
22 J. Moon, S. Yoon, Y. S. Lim, and W. Choi, Opt. Express **28**, 4463 (2020), arXiv: 1909.00499.
23 R. Kodama, K. Okada, and Y. Kato, Rev. Sci. Instrum. **70**, 625 (1999).
24 Y. C. Eldar, and G. Kutyniok, *Compressed Sensing : Theory and Applications* (Cambridge University Press, Cambridge, New York, 2012).
25 J. Liang, P. Wang, L. Zhu, and L. V. Wang, Nat. Commun. **11**, 5252 (2020).
26 P. Wang, J. Liang, and L. V. Wang, Nat. Commun. **11**, 1 (2020).
27 L. Fan, X. Yan, H. Wang, and L. V. Wang, Sci. Adv. **7** (2021).
28 J. Liang, C. Ma, L. Zhu, Y. Chen, L. Gao, and L. V. Wang, Sci. Adv. **3**, e1601814 (2017).
29 J. Liang, L. Gao, P. Hai, C. Li, and L. V. Wang, Sci. Rep. **5**, 15504 (2015).
30 J. C. Jing, X. Wei, and L. V. Wang, Nat. Commun. **11**, 2059 (2020).
31 Y. Liu, X. Yuan, J. Suo, D. J. Brady, and Q. Dai, IEEE Trans. Pattern Anal. Mach. Intell. **41**, 2990 (2019).
32 X. Yuan, Y. Liu, J. Suo, and Q. Dai, in: *Plug-and-Play Algorithms for Large-Scale Snapshot Compressive Imaging: Proceedings of the IEEE/CVF Conference on Computer Vision and Pattern Recognition (CVPR)*, Seattle, 2020, pp. 1447-1457.
33 Y. Lai, Y. Xue, C. Y. Côté, X. Liu, A. Laramée, N. Jaouen, F. Légaré, L. Tian, and J. Liang, Laser Photon. Rev. **14**, 2000122 (2020).
34 Y. Sun, B. Wohlberg, and U. S. Kamilov, IEEE Trans. Comput. Imag. **5**, 395 (2019).
35 Z. Xu, B. Shen, L. Zhang, J. Xu and W. Gong, Plasma Phys. Control. Fusion **63**, 035013 (2021).
36 A. Denoeud, L. Chopineau, A. Leblanc, and F. Quéré, Phys. Rev. Lett. **118**, 33902 (2017).
37 L. Allen, M. W. Beijersbergen, R. J. C. Spreeuw, and J. P. Woerdman, Phys. Rev. A **45**, 8185 (1992).
38 G. Q. Zhou, Y. J. Cai, and C. Q. Dai, Sci. China-Phys. Mech. Astron. **56**, 896 (2013).
39 Z. Zhong, W. Gong, H. Jiang, H. Gu, X. Chen, and S. Liu, Appl. Sci.

10, 1584 (2020).

40   K. H. Hong, J. H. Sung, Y. S. Lee, and C. H. Nam, Opt. Commun. **213**, 193 (2002).

41   B. Wahlberg, S. P. Boyd, M. Annergren, and Y. Wang, in: *An ADMM Algorithm for a Class of Total Variation Regularized Estimation Problems: Proceedings of the 16th IFAC Symposium on System Identification (SYSID 2012)*, Brussels, 2012, pp. 83-88.

42   S. H. Chan, X. Wang, and O. A. Elgendy, IEEE Trans. Comput. Imag. **3**, 84 (2017).

43   C. Yang, F. Cao, D. Qi, Y. He, P. Ding, J. Yao, T. Jia, Z. Sun, and S. Zhang, Phys. Rev. Lett. **124**, 23902 (2020).

44   N. Otsu, IEEE Trans. Syst. Man Cybern. **9**, 62 (1979).

45   N. Ding, Y. Liu, Y. Jin, and M. Zhu, in: *Image Registration Based on Log-Polar Transform and SIFT Features: Proceedings of the International Conference on Computational and Information Sciences (ICCIS)*, Chengdu, 2010, pp. 749-752.

46   C. Yang, D. Qi, F. Cao, Y. He, J. Yao, P. Ding, X. Ouyang, Y. Yu, T. Jia, S. Xu, Z. Sun, and S. Zhang, Phys. Rev. Appl. **13**, 24001 (2020).

47   W. Liu, Y. Liu, J. Q. Huang, G. R. Huang, Y. Zhang, and W. L. Fu, Front. Lab. Med. **2**, 127 (2018).

48   K. Miyamoto, K. Sano, T. Miyakawa, H. Niinomi, K. Toyoda, A. Vallés, and T. Omatsu, Opt. Express **27**, 31840 (2019), arXiv: 1912.08979.

49   Y. Shen, X. Wang, Z. Xie, C. Min, X. Fu, Q. Liu, M. Gong, and X. Yuan, Light Sci. Appl. **8**, 90 (2019).